ACS OMEGA

Open Access

http://pubs.acs.org/journal/acsodf

Article

Detergent-Triggered Membrane Remodelling Monitored via Intramembrane Fluorescence Dequenching

Claudia M. F. Andrews, Christopher M. Hofmair, Lauryn Roberts, Emily James, Katie Morris, Kevin Kramm, Mark C. Leake, Yue Wang, and Steven D. Quinn*

Cite This: https://doi.org/10.1021/acsomega.5c10435

Read Online

ACCESS | Metrics & More | Article Recommendations | Supporting Information

ABSTRACT: Detergent-induced membrane solubilization is important for several biotechnological applications including membrane protein isolation, cell lysis and virus inactivation. The thermodynamic details of the underlying process have been previously examined, but the mechanistic details remain largely underexplored owing in part to a lack of suitable technologies capable of assessing nanoscopic membrane disruption events. Key open questions include: how do detergents remodel the membrane structure at subsolubilizing concentrations? And what is the sequence of morphological transitions that lead up to solubilization? Here, we introduce a single-color assay based on the fluorescence dequenching of membrane-integrated fluorophores as a sensitive and generalizable tool to probe nanoscale membrane remodelling events induced by detergents. We demonstrate, using fluorescence spectroscopy and time-correlated single photon counting, that the widely used detergent Triton X-100 triggers substantial morphological changes at concentrations below its critical micellar concentration. Moreover, by taking advantage of single vesicle fluorescence lifetime imaging and scanning electron microscopy, we reveal that the swelling step involves a morphological transition from spherical vesicles to toroidal structures, providing direct evidence for detergent-driven membrane reorganization prior to solubilization. Our findings support and refine a multistep model of detergent-induced membrane solubilization, positioning fluorescence dequenching as a tool for detecting conformational intermediates. We show that the fluorescence dequenching approach performs robustly across multiple cyanine-based probes and experimental conditions and its nanoscale sensitivity provides a platform from which to interrogate membrane perturbations induced by a wide variety of molecular disruptors, including those with important biomedical significance.

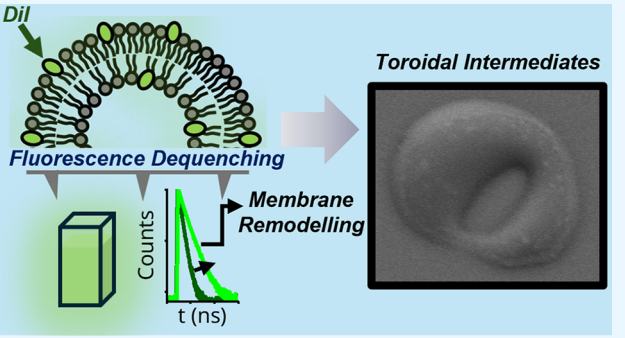

INTRODUCTION

Detergent-membrane interactions are critical for a variety of applications including membrane protein extraction and isolation,[1] virus inactivation,[2,3] cellular drug delivery,[4] forming niosomes in vaccine formulations,[5] and for constructing artificial membranes and supported lipid bilayers.[6] In this context, Triton X-100 (TX-100) is widely used as a gold-standard nonionic detergent due to its ability to gently solubilize membrane proteins while maintaining their structure and function, making it ideal for biochemical and structural studies.[7,8] Its relatively low critical micellar concentration (CMC) of ∼0.2−0.3 mM[8−10] and mild impact on protein conformation[11] make it particularly suitable for studies requiring intact protein−lipid interactions, unlike stronger ionic detergents which can disrupt protein functionality. However, the mechanistic details of the TX-100 membrane interaction have remained underexplored, owing in part to a lack of suitable tools and technologies capable of assessing the interaction. In particular, there remains limited understanding of how detergent molecules initiate structural rearrangements on the nanoscale, what intermediate membrane conformations precede micellization, and how these effects depend on the detergent type, concentration and membrane composition.

In recent years, the emergence of model-membrane systems such as lipid vesicles and supported bilayers[6] has helped researchers explore the underlying details. Previous biochemical approaches investigating TX-100 interactions demonstrated, for example, that the solubilization rate and effectiveness of the detergent depend on the lipid phase, absolute detergent concentration and the lipid composition.[12−17] These results, and others, broadly confirm that TX-100 is particularly effective at solubilizing phosphocholine (PC) rich membranes, with solubilization kinetics generally faster in the fluid phase. Gel-

Received: October 7, 2025
Revised: November 24, 2025
Accepted: December 22, 2025

phase membranes, in contrast, require higher TX-100 concentrations for complete solubilization, especially as the lipid chain length increases.[15] Additionally, TX-100s action is inhibited by membrane cholesterol, likely due to the formation of detergent-rich regions that may function as lipid rafts.[16,18] Molecular dynamics simulations[18−20] and phase contrast microscopy experiments[17] have also provided insights into early stage permeabilization events, but despite such advancements, challenges remain in dissecting the process at each solubilization stage. Moreover, there is also demand for new tools that can monitor the impact of TX-100 on submicron sized membrane systems that are beyond the reach of conventional diffraction-limited optical microscopy approaches.

Nevertheless, based on these experiments a global three-step model has been proposed to describe TX-100-induced membrane solubilization: (1) detergent monomers saturate the membrane, (2) mixed detergent-lipid micelles form leading to membrane fragmentation, and (3) mixed micelles are released into solution.[12,21] Membrane permeabilization assays based on the influx of calcium into lipid vesicles encapsulating fluorescent indicators have also revealed that transient defects and micropores form on intact vesicles during the process.[22] We also recently showcased dual-color fluorescence assays based on Förster resonance energy transfer (FRET) between membrane-embedded fluorophores, to support a refined model in which both structural changes and membrane fusion take place prior to step 3.[23−25] However, FRET-based approaches are not without their limitations. For example, FRET signatures can be challenging to interpret in heterogeneous mixtures as changes in the probe orientation, lipid packing density or local membrane dynamics all influence the Förster distance.[26]

Inspired by these insights, we now introduce a single-color assay based on the fluorescence dequenching of membrane-embedded probes as a powerful, but straightforward means to probe and quantify detergent-induced membrane perturbations via enhancements in both fluorescence intensity and probe lifetime. In contrast to FRET, which depends on the distance-dependent energy transfer of donor−acceptor pairs, fluorescence self-quenching arises when identical fluorophores are in close proximity, leading to nonradiative decay pathways. Upon membrane expansion or dilution of the fluorophore density, the nonradiative decay pathways are reduced, resulting in a measurable increase (dequenching) of fluorescence emission intensity and lifetime. We demonstrate that the dequenching approach reports on the distance between membrane-embedded fluorophores, and can be implemented using a range of dyes and experimental conditions. We benchmark the dequenching approach against the existing FRET-based strategy and use it to explore the structural integrity of PC-rich vesicles in response to TX-100. In conjunction with single particle imaging approaches, our observations confirm that TX-100 triggers vesicle swelling and morphological transitions, even at concentrations below the reported CMC, prior to complete solubilization. We expect the fluorescence dequenching approach to have far-reaching applications in quantitatively reporting on membrane disruption events induced by a wide variety of molecular disruptors including surfactants and proteins with important biomedical significance.

METHODS

Materials

1-palmitoyl-2-oleoyl-*glycero*-3-phosphocholine (POPC) lipids suspended in chloroform, TX-100, sodium dodecyl sulfate (SDS) and Tween 20 were purchased from Merck. All stock detergent solutions were prepared in 50 mM Tris buffer (pH 8) prior to each use. The lipophilic membrane stains DiI ($DiIC_{18}(3)$), DiD ($DiIC_{18}(5)$) and DiO ($DiOC_{18}(3)$) were purchased from ThermoFisher Scientific. All lipid and membrane stain stocks were stored at −20 °C prior to use. All samples were used directly from the manufacturer without any additional purification.

Large Unilamellar Vesicle Preparation

POPC vesicles incorporating DiI, DiD or DiO were prepared via the extrusion method. Briefly, the lipids and membrane stains were mixed in chloroform at the levels specified in the main text and the solvent was evaporated under gentle nitrogen flow. The resulting lipid film was then resuspended in 50 mM Tris buffer (pH 8) and vortexed. Unilamellar vesicles were then prepared by passing the solutions at least 21 times through a Mini Extruder (Avanti Research) containing a polycarbonate membrane filter of defined pore size.

Fluorescence Spectroscopy

Fluorescence emission spectra were acquired under magic angle conditions using a FluoTime 300 (PicoQuant) spectrophotometer. Spectra from vesicles incorporating DiI, DiO and DiD in solution were recorded using excitation wavelengths of 532, 485 and 640 nm, respectively. All experiments were performed in 50 mM Tris buffer (pH 8) with a final POPC concentration of 30 μg/mL.

Time Correlated Single Photon Counting

Time-resolved fluorescence spectroscopy on labeled vesicles in solution was also performed using a FluoTime 300 spectrophotometer equipped with time-correlated single photon counting electronics and a hybrid PMT detector (PMA Hybrid 07, PicoQuant). Time-resolved fluorescence decays were measured under magic angle conditions using pulsed excitation at 532, 485 and 640 nm for samples containing DiI, DiO and DiD, respectively. In all cases, repetition rates of 50 MHz were used. Time-resolved fluorescence decays at the maximal intensity emission wavelengths were collected until 10^4 photon counts accumulated at the decay maximum. Fluorescence decay curves were then fitted by iterative reconvolution of the instrument response function and the observed fluorescence decay using a biexponential decay function of the form $I_t = ae^{-t/\tau_1} + be^{-t/\tau_2}$, where I_t is the intensity at time, t, normalized to the intensity at $t = 0$, τ_1 and τ_2 represent the fluorescence lifetimes of fast and slow decay components, and a and b are the associated fractional amplitudes. We note that biexponential fits were applied based on the convergence of the reduced chi-squared to the experimental data. All experiments were performed in 50 mM Tris buffer (pH 8) with a final POPC concentration of 30 μg/mL. The variation in amplitude weighted average lifetimes was fitted to a Hill model of the form

$$\tau_{av} = A + B\frac{[\text{TX-100}]^n}{k^n + [\text{TX-100}]^n}$$

https://doi.org/10.1021/acsomega.5c10435
ACS Omega XXXX, XXX, XXX−XXX

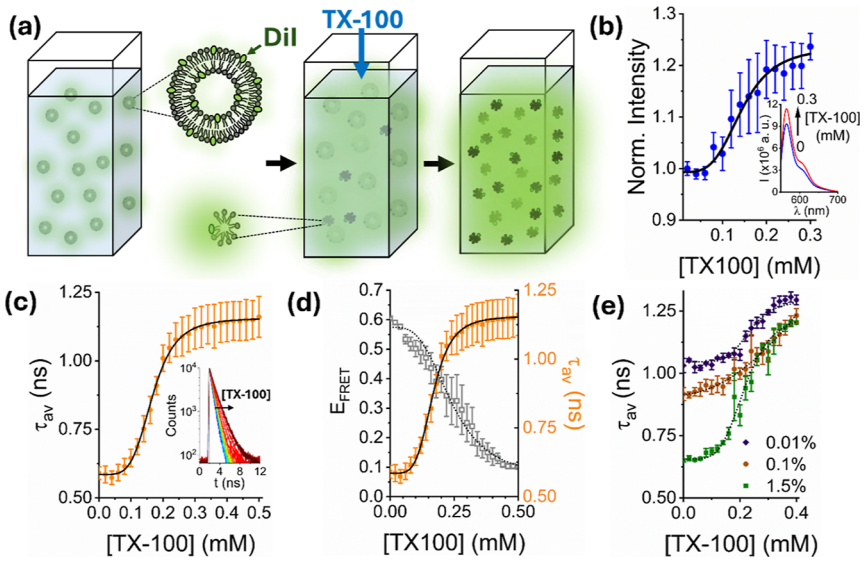

Figure 1. TX-100 induced vesicle solubilization monitored by fluorescence dequenching. (a) Schematic illustration of the assay. Injection of TX-100 into solution containing DiI-labeled POPC vesicles induces vesicle solubilization, triggering an increase in the relative DiI−DiI distance and dequenching. (b) Variation in the integrated fluorescence emission intensity of 200 nm sized vesicles containing 1% DiI in the absence and presence of TX-100. Inset: representative variation in fluorescence emission spectra in the absence and presence of 0.3 mM TX-100. The solid black line represents a Hill model fit (χ^2 = 0.92) with a half maximal concentration constant, k, of 0.14 ± 0.03 mM (n = 3.9 ± 0.2). (c) The corresponding variation in τ_{av} across the titration with corresponding Hill fit (solid black line; χ^2 = 0.99; k = 0.17 ± 0.01 mM, n = 4.6 ± 0.2). Inset: the corresponding fluorescence decays and instrumental response function (gray). (d) Variation in τ_{av} associated with vesicles containing 1% DiI as a function of TX-100 concentration compared to the variation in E_{FRET} obtained from vesicles containing 0.1% DiI and 0.1% DiD under identical conditions. The dashed line represents the corresponding Hill model (χ^2 = 0.99; k = 0.24 ± 0.01 mM, n = 3.3 ± 0.4). (e) Variation in τ_{av} and Hill fits (dashed lines) associated with vesicles containing 0.01% (χ^2 = 0.98; k = 0.23 ± 0.01 mM, n = 5.7 ± 0.9), 0.1% (χ^2 = 0.99; k = 0.21 ± 0.01 mM, n = 1.8 ± 0.4), and 1.5% DiI (χ^2 = 0.99; k = 0.22 ± 0.01 mM, n = 4.6 ± 0.2) as a function of TX-100. In all cases, data points represent the mean values from three separate experimental runs and error bars denote the standard error of the mean.

where A and B are the measured lifetimes at the start and end of the titration, k is the half-maximal concentration constant and n is the Hill coefficient.

Single Vesicle Fluorescence Lifetime Imaging (svFLIM)

svFLIM measurements were performed using a Luminosa single photon counting confocal microscope (PicoQuant) using the dedicated FLIM workflow available in the system. Briefly, 50 μL droplets of vesicles in solution were pipetted onto high precision cover glasses coated in 1% poly L-lysine. Excitation was provided by a pulsed diode laser emitting at 532 nm with pulse width of 76 ps and repetition rate of 20 MHz (LDH-D-FA-530L) at an output power of 0.5 μW (measured after the main dichroic mirror). Images were acquired with a FLIMbee galvo scanner. The emission was collected with a 60 ×1.20 numerical aperture objective lens (Evident). A single-photon avalanche diode (SPAD; Excelitas AQRH-14) and suitable optical filters were used to detect fluorescence photons in the spectral range between 545 and 615 nm. Photon detection events were time-correlated to excitation pulses using a time-correlated single-photon counting device (MultiHarp 150 8P, PicoQuant). Fluorescence decays were fitted to biexponential decays using the Luminosa software (PicoQuant).

Scanning Electron Microscopy (SEM)

SEM was performed using a JEOL JSM 7800-F system operating at 5 kV. Vesicles were prepared in 50 mM Tris (pH 8) containing TX-100 at the specified concentrations, diluted in deionized water, and vortexed prior to imaging. Two μL volumes of the vesicle solution were then added to a clean silicon substrate and the solution evaporated. Reference samples without TX-100 were prepared under the same conditions. All substrates were then sputtered with an 8 nm copper layer for charge dissipation purposes before loading into the microscope. Vesicle diameters were determined using ImageJ, where automated analysis of black and-white binary images enabled separation of regions of white pixels against a dark background. Vesicle circularity was measured via $4p(A/p^2)$, where A is the observed area and p is the perimeter.

Dynamic Light Scattering (DLS)

Hydrodynamic radii of POPC vesicles labeled with 1% DiI in the absence and presence of TX-100 were measured using a Zetasizer mV DLS instrument (Malvern Instruments) equipped with a 632.8 nm laser line. A final lipid concentration of 30 μg/mL in 50 mM Tris buffer (pH 8) was used in all cases. The correlation of scattered intensity fluctuations yielded the diffusion coefficients as previously described.[27]

Fluorescence Correlation Spectroscopy (FCS)

FCS measurements were performed on POPC vesicles labeled with 1% DiI at room temperature using an EI-FLEX FCS spectrometer (Exciting Instruments) equipped with a 520 nm excitation line (LuxX, Omicron). Photons were recorded on an avalanche photodiode (AQRH-14, Excelitas) and correlation curves were generated and fitted using pulsed interleaved excitation analysis with MATLAB (PAM) software.[28] Correlation curves, $G(\tau)$ were best fitted to a model of the form

$$G(\tau) = \frac{1}{N\sqrt{8}}\left(1 + \frac{T}{1-T}e^{-\tau/\tau_T}\right)\left(1 + \frac{4D\tau}{\omega_r^2}\right)^{-1}\left(1 + \frac{4D\tau}{\omega_z^2}\right)^{-1/2} + y_0$$

https://doi.org/10.1021/acsomega.5c10435
ACS Omega XXXX, XXX, XXX−XXX

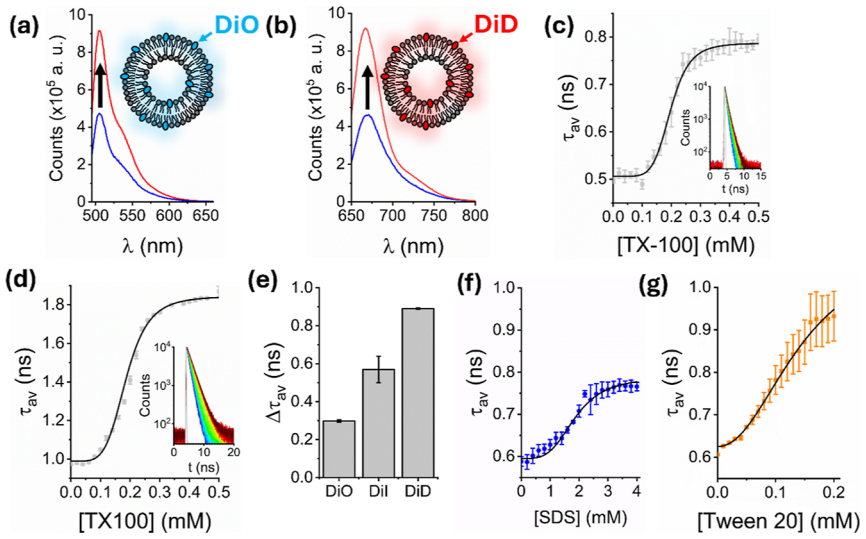

Figure 2. Expanding the scope of fluorescence dequenching. Variation in the integrated fluorescence emission intensity of 200 nm sized POPC vesicles containing (a) 1% DiO and (b) 1% DiD in the absence (blue) and presence (red) of 0.3 mM TX-100. Insets: schematic illustrations of the vesicles. Representative variation in τ_{av} as TX-100 was progressively added to vesicles containing (c) 1% DiO and (d) 1% DiD. Insets: the corresponding time-resolved fluorescence decays. The solid black lines represent Hill fits to the experimental data ($\chi^2 = 0.99$; $k = 0.19 \pm 0.01$ mM in both cases with $n = 6.1 \pm 0.5$ (DiO) and $n = 4.9 \pm 0.3$ (DiD)) and the solid gray lines indicate the instrumental response functions. (e) Comparative bar plot summarizing the relative magnitude of the dequenching signal between the start and end of the titration as a function of dye at 1%. (f) Representative variation in τ_{av} obtained from POPC vesicles labeled with 1% DiI in the absence and presence of SDS with Hill fit shown in the solid black line ($\chi^2 = 0.96$; $k = 1.9 \pm 0.01$ mM, $n = 3.7 \pm 0.4$). (g) The corresponding τ_{av} data and fit ($\chi^2 = 0.96$; $k = 0.14 \pm 0.09$ mM. $n = 2.1 \pm 0.5$) obtained from vesicles containing 1% DiI in the presence of Tween 20. Error bars represent the standard error of the mean from three separate experimental runs.

where N is the number of fluorophores in the excitation volume, D is the diffusion coefficient, ω_r is the radial waist of the excitation volume, ω_z is the axial waist of the excitation volume, τ_T is the triplet component correlation time, T is the triplet component amplitude and y_0 is the offset. Control experiments performed independently on Cy3B at 1 nM revealed radial and axial waists of 0.23 and 3.31 μm, respectively.

RESULTS AND DISCUSSION

Fluorescence Dequenching as a Probe of TX-100 Induced Vesicle Solubilization

Large unilamellar vesicles composed of 99% POPC lipids and 1% of the lipophilic cyanine derivative DiI were first prepared as outlined in the Methods, and are schematically illustrated in Figure 1a. As previously reported, POPC is abundantly found in mammalian membranes and was used here to provide a synthetic mimetic.[29] Here, a mean DiI−DiI separation distance of <2 nm was achieved, leading to a high level of fluorescence self-quenching. We hypothesized that detergent-induced structural rearrangements, such as swelling, fragmentation and lysis, would lead to nanoscale increases in the average dye−dye separation distance that, in turn, could trigger fluorescence dequenching and quantifiable changes to the mean DiI fluorescence emission intensity and lifetime as illustrated in Figure 1a.

200 nm-sized vesicles incorporating DiI were prepared via extrusion, and their steady-state fluorescence emission spectra were recorded as a first step to characterize their interaction with TX-100 above and below the reported CMC. As the concentration of TX-100 was progressively increased, a 24 ± 2% increase in the integrated DiI emission intensity was observed across the titration, consistent with a dequenching mechanism (Figure 1b). To confirm a dequenching process, we also evaluated the amplitude-weighted average lifetime, τ_{av}, of membrane-bound DiI using time-correlated single photon counting. Here, τ_{av} progressively increased with TX-100 concentration consistent with a progressive dequenching of DiI (Figure 1c). In all cases, and in line with previous observations,[23] the time-resolved fluorescence decays were best fit to a biexponential decay model after reconvolution with the instrument response function, representing variations in the dye's local environment.[22] In the absence of TX-100 we recorded a $\tau_{av} = 0.59 \pm 0.04$ (±SD) ns, representative of quenched DiI. A 2-fold increase in τ_{av} was then observed as TX-100 was titrated above and below the CMC (Figure 1c). A Hill model was applied as an empirical means to capture the sigmoidal dependence of fluorescence lifetime and intensity on detergent concentration. In this context, variations in τ_{av} revealed a half-maximal concentration of 0.17 ± 0.01 mM, which we note is comparable in magnitude to the reported CMC. Upon further inspection, we found that both fast and slow lifetime components increased across the titration, though their relative amplitude weighted percentage contributions remained largely invariant (Figures S1 and S2). Comparable responses were obtained for vesicles of ∼30 nm, ∼400 nm and ∼1000 nm diameter containing 1% DiI, where half-maximal concentrations of 0.22 ± 0.01, 0.18 ± 0.01 mM and 0.25 ± 0.01 mM were observed (Figure S3), indicating that vesicle size within the range tested exerts minimal influence on the detergent−membrane interaction. In all cases, the fitted Hill coefficients were in the range 3.6−4.6, consistent with a cooperative binding or disruption process in which insertion of TX-100 molecules facilitates subsequent membrane perturbation. The concentration-dependent increase in τ_{av} also exhibited a similar half-maximal concentration to that obtained from the solubilization of 200 nm-sized vesicles labeled with 0.1% DiI and 0.1% DiD evaluated using the previously

https://doi.org/10.1021/acsomega.5c10435
ACS Omega XXXX, XXX, XXX−XXX

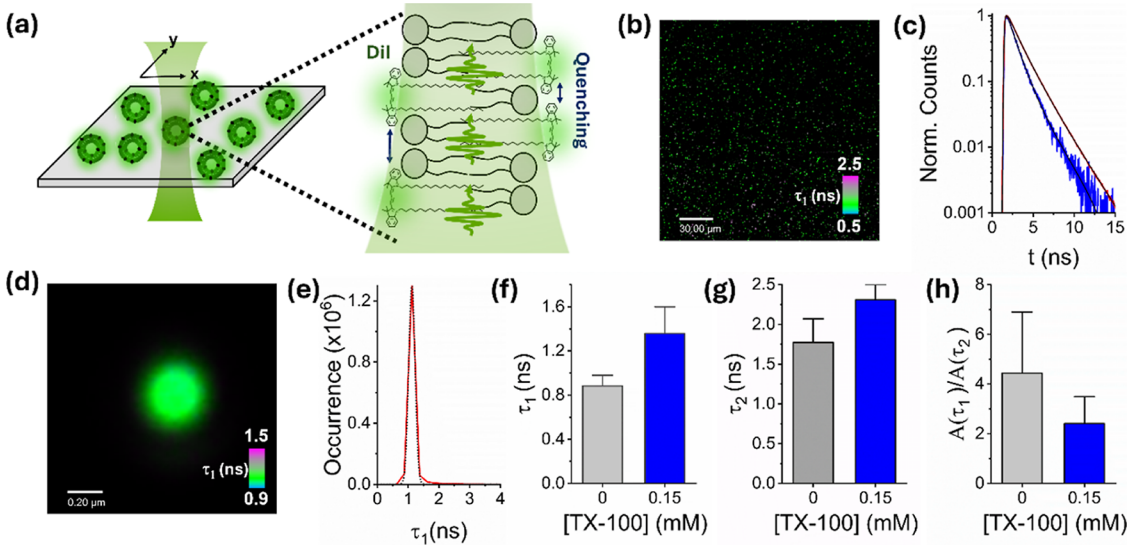

Figure 3. TX-100 induces the structural remodelling of single immobilized vesicles. (a) Schematic illustration of the FLIM approach. Individual vesicles incorporating DiI are immobilized and spatially isolated on a surface, where they are excited by pulsed excitation in a confocal geometry. (b) Representative FLIM image of surface-immobilized POPC vesicles incorporating 1% DiI showing variations in fast component, τ_1 across the field of view. (c) Variation in TCSPC FLIM decays recorded from vesicles in the absence (blue) and presence of 0.15 mM TX-100 (red). Solid black lines represent biexponential fits after reconvolution with the instrument response function. (d) Representative FLIM image of a single DiI-vesicle (no detergent) showing variations in fast component, τ_1 across the structure. (e) The corresponding distribution of τ_1 values across the vesicle surface. The dotted black line corresponds to a Gaussian fit with center of 1.12 ns, full width at half-maximum of 0.2 ns and $\chi^2 = 0.99$. Comparative bar charts summarizing the mean variations in (f) τ_1, (g) τ_2 and (h) $A(\tau_1)/A(\tau_2)$ obtained from $N = 5$ randomly selected immobilized vesicles. Error bars correspond to the standard deviations.

demonstrated FRET-based sensing approach[22−24] (Figure 1d). Here, a TX-100 induced distance increase between donor (DiI) and acceptor (DiD) probes leads to a progressive reduction in the apparent FRET efficiency, E_{FRET}, across the titration. The anticorrelation observed between the τ_{av} signal obtained from the single-color assay and the apparent FRET efficiency from the dual-color approach provides confidence that the dequenching approach quantitatively reports on perturbations on the nanoscale. Unlike the FRET-based approach, however, the dequenching assay avoids donor−acceptor stoichiometry dependence and spectral bleed-through, enabling a direct readout of membrane disruption. We also note that the amount of DiI per vesicle was optimized (1%) to maximize the magnitude of the dequenching response across the interaction. In this context, the initial amplitude-weighted lifetime progressively increased toward a dequenched state as the dye concentration was reduced to 0.1% and 0.01%, respectively (Figure 1e). The initial lifetime values were, however, comparable when the vesicles contained 1% and 1.5% DiI. In all cases, and in line with the data shown in Figure 1c, a progressive increase in the probe lifetime was observed, even at concentrations below the reported CMC, and a final end-point (1.2−1.3 ns) was reached.

Fluorescence Dequenching as a Generalizable Assay

To assess whether the fluorescence dequenching approach was applicable beyond the DiI system, we also evaluated the response of 200 nm sized vesicles containing DiO and DiD. Like DiI, DiO and DiD are long-chain dialkylcarbocyanines with emission excitation/emission maxima at 484/501 nm and 644/665 nm, respectively.[30] As the concentration of TX-100 was progressively increased, the integrated emission intensity of vesicles containing 1% of each dye also progressively increased, in line with our previous observations (Figure 2a,b). In both cases, the fluorescence decay curves also shifted to longer decay times as evidenced by a progressive increase in the τ_{av} signatures (Figure 2c,d). Here, the initially quenched lifetimes of DiO (0.51 ± 0.01 ns) and DiD (0.97 ± 0.01 ns) increased to 0.79 ± 0.01 ns and 1.87 ± 0.03 ns respectively as TX-100 was injected above and below the CMC. In both cases the half-maximal concentration requirements to achieve solubilization were identical (k = 0.19 ± 0.01 mM) and in agreement with our observations from DiI. We note that the magnitude of the lifetime changes between the start- and end-point of the titration increased in the order DiO > DiI > DiD (Figure 2e), which we speculate might reflect differences in the dye−lipid interaction strength, the extent of dye interactions within the membrane, and/or variations in the degree of dye insertion into the lipid bilayer. For example, molecular dynamics simulations have previously suggested that the headgroup of DiI is distributed between 0.3−2 nm from the center of a dipalmitoylphosphatidylcholine (DPPC) bilayer and below the phospholipid headgroup region,[31] and spectroscopic measurements indicate that DiO's insertion efficiency is strongly modulated by the lipid microenvironment.[32] Though direct comparison of each dye's insertion depth within a POPC bilayer remains to be elucidated, variations in the dye conjugation length and hydrophobicity may directly influence the self-quenching efficiency, and thus the observed differences in the dequenching magnitude.

Having established that the dequenching assay operates across a range of fluorescent probes, we next evaluated the response of DiI loaded POPC vesicles to other surfactants including sodium dodecyl sulfate (SDS) and Tween 20 to gauge its utility across a range of molecular disruptors. Unlike TX-100, SDS is an anionic detergent with a linear alkyl chain, a sulfate headgroup, and CMC of ∼6−8 mM, making it highly denaturing.[24] Tween 20, like TX-100, is also nonionic, with a polyoxyethylene sorbitan ester structure, a CMC of ∼0.06 mM,

https://doi.org/10.1021/acsomega.5c10435
ACS Omega XXXX, XXX, XXX−XXX

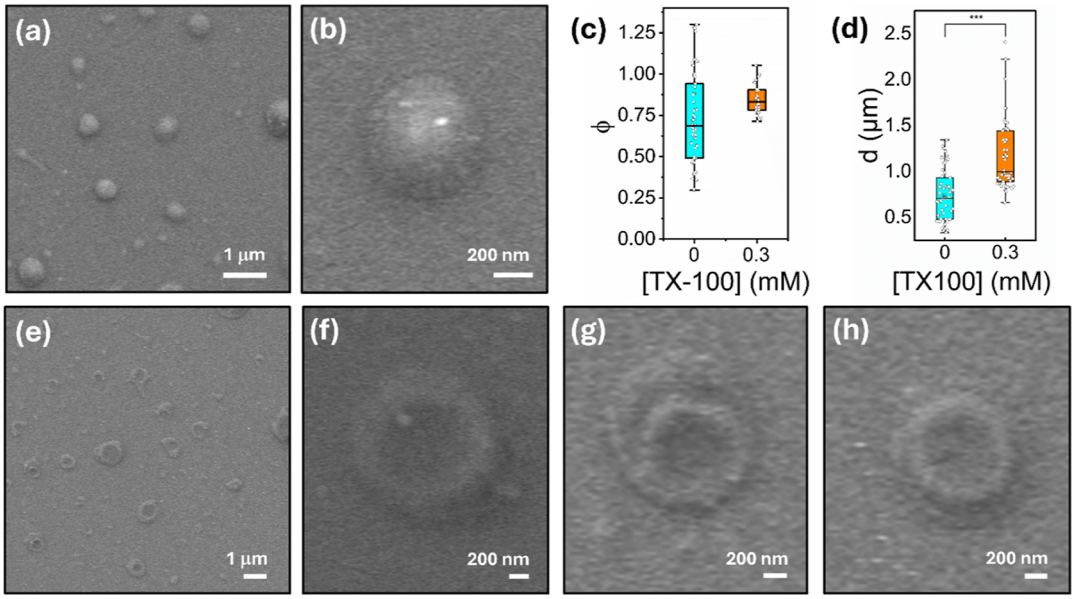

Figure 4. TX-100 induces vesicle swelling and morphological transitions. (a,b) Representative SEM images of freshly prepared vesicles in the absence of TX-100. Comparative bar plots summarizing the variation in (c) circularity and (d) particle diameter for vesicles in the absence and presence of 0.3 mM TX-100 ($N = 50$). ***$p < 0.05$ as determined by an unpaired sample t-test. (e−h) Representative SEM images of freshly prepared vesicles in the presence of 0.3 mM TX-100.

and is generally considered mild upon comparison with SDS.[22] Under both conditions, the initial amplitude-weighted average lifetimes were comparable to those previously reported, indicating reproducibility of the starting material. Upon addition of SDS, we observed a progressive increase in τ_{av} from 0.59 ± 0.01 to 0.77 ± 0.01 ns, with a half-maximal concentration constant of 1.9 mM (Figure 2f). By contrast, the lifetime increased to 0.93 ± 0.01 ns upon addition of only 0.2 mM Tween 20 (Figure 2g). The relative difference in the magnitude of the fluorescence lifetime shift between the two detergents could arise because of distinct interactions with the vesicle membrane and/or variations in the final micellar forms. For example, SDS is an anionic surfactant that likely disrupts membrane packing to a lesser extent than the nonionic surfactant Tween 20, which may integrate more effectively into the bilayer and alter the local environment of DiI. SDS and Tween 20 also form micelles with distinct structural characteristics; SDS generally induces small, spherical mixed detergent-lipid micelles which have a high negative surface charge and tight packing, whereas Tween 20 induced micelles are larger and less uniformly shaped with the detergent arranged in a more loosely packed environment.[33,34] Nevertheless, in all cases it is striking to note that the dequenching signal occurs at concentrations below the respective detergent's critical micellar concentration, indicating that the assay is sensitive to conformational changes such as vesicle swelling which occurs before solubilization and release of mixed detergent-lipid micelles.

Triton X-100 Triggers Vesicle Swelling and Morphological Transitions

To assess whether the observed variations in fluorescence intensity and lifetime could be assigned to vesicle swelling, we performed an array of single-vesicle imaging experiments. We first performed fluorescence lifetime imaging (FLIM) to assess the lifetime distributions from single DiI-labeled vesicles. Here, ∼200 nm-sized POPC vesicles containing DiI at 1% were nonspecifically attached to a poly L-lysine-coated coverslip and the variation in lifetime distribution across the surface, and across single vesicles, was monitored before and after the addition of TX-100 at subsolubilizing concentrations (Figure 3a). It is important to note that the immobilized vesicles were also spatially isolated on the surface, minimizing the possibility of fusion. In the absence of TX-100, we observed ∼200−300 fluorescent foci per 190 × 190 μm^2 field of view, representing individual nonspecifically bound vesicles (Figure 3b). In line with our prior ensemble-based measurements, the distribution of lifetime values from hundreds of surface-immobilized vesicles also fitted well to a biexponential model comprising fast (0.76 ± 0.16 ns) and slow (2.01 ± 0.14 ns) components and an amplitude-weighted average lifetime of 0.99 ± 0.3 ns (Figure 3c). As 0.15 mM TX-100 was added, we observed a substantial increase in both lifetime components (τ_1 = 1.32 ± 0.09 ns and τ_2 = 2.27 ± 0.04 ns), and τ_{av} increased by ∼68% to 1.67 ± 0.34 ns (Figure 3c) while the total number of fluorescent foci per field of view, and therefore the number of vesicles on the surface, remained largely invariant (Figure S4). The lifetime increase observed across single vesicles at low TX-100 concentrations could not therefore be attributed to complete solubilization of the vesicles or lipid loss, but rather structural changes taking place within the intact vesicles. We assigned the dequenching signal observed here to detergent-induced remodelling of the membrane that involves vesicle swelling and/or morphological transitions with minimal loss of lipid material to the bulk solution. To support this assertion, we also performed both DLS and FCS measurements on freely diffusing vesicles. In both cases, the vesicle's hydrodynamic radius is inversely proportional to the diffusion coefficient according to the Stokes−Einstein law, and so we reasoned that both techniques could offer insight into detergent-induced vesicle swelling. In the absence of TX-100, DLS revealed a vesicle radius of 90.4 ± 0.2 nm that increased by ∼13% in the presence of 0.15 mM TX-100, consistent with combinations of vesicle swelling and/or fusion in the ensemble (Figure S5). By performing FCS measurements, where the vesicle concen-

https://doi.org/10.1021/acsomega.5c10435
ACS Omega XXXX, XXX, XXX−XXX

tration was only ∼10 pg/mL, thereby mitigating against fusion, we identified a decrease in the diffusion coefficient from 0.88 $\mu m^2\ s^{-1}$ to 0.65 $\mu m^2\ s^{-1}$ in the presence of 0.15 mM TX-100 (Figure S5), consistent with both a 16% increase in vesicle size and a mechanism of interaction that involves vesicle swelling. We note that the distribution of individual lifetime components obtained across single vesicles was generally Gaussian distributed with a full-width at half-maximum of ∼0.2 ns, indicating a lack of fused, aggregated or significantly perturbed species on the surface (Figure 3d,e). Our observations were also reflected when random sampling of the mean component lifetimes per vesicle revealed a 1.5-fold increase in τ_1 (Figure 3f) and a 1.3-fold increase in τ_2 (Figure 3g). Furthermore, the corresponding ratio of amplitudes associated with the fast and slow components ($A(\tau_1)/A(\tau_1)$) decreased from 4.4 ± 1.1 to 2.4 ± 0.8 (Figure 3h), indicating that TX-100 alters the lipid microenvironment, disrupting dye−dye interactions that favor the fast lifetime component.

To further support the detergent-induced swelling of intact vesicles, and to assess whether or not morphological transitions were taking place, we also probed vesicle sizes and structures in response to TX-100 via scanning electron microscopy. Here, we assessed the size distribution of vesicles extruded through polycarbonate membrane filters of 1 μm pore diameter to facilitate visualization of detergent-induced morphological transitions at the single-vesicle level. SEM micrographs revealed that freshly prepared vesicles were predominantly spherical (mean circularity = 0.73; standard deviation = 0.28, standard error of the mean = 0.04) (Figure 4a−c) with a mean diameter of 750 nm (standard deviation = 275 nm, standard error of the mean = 40 nm, N = 50) (Figure 4d), in line with solution-based DLS measurements that indicated a log-normal distribution of particles centered on a hydrodynamic radius of 470 ± 2 nm (Figure S5). After treatment with 0.3 mM TX-100, the vesicles were also spherical (mean circularity = 0.84; standard deviation = 0.09, standard error of the mean = 0.02) (Figure 4d,e) but the size distribution broadened, and the mean diameter was centered on 1173 nm (standard deviation = 379 nm, standard error of the mean = 54 nm, N = 50), representing a 56% increase. DLS measurements also supported a TX-100 induced radius increase to 608 ± 7 nm (Figure S5). At the 0.05 level, an unpaired sample t-test indicated that the difference between population means is significantly different. We also note that exposure to TX-100 induced a morphological transition from intact spherical vesicles to toroidal-like structures in 75% of species imaged (Figure 4e−h). Complementary FCS measurements on the freely diffusing vesicles also revealed a decrease in diffusion coefficient from 0.23 $\mu m^2\ s^{-1}$ to 0.13 $\mu m^2\ s^{-1}$ in the presence of 0.15 mM TX-100, consistent with swelling behavior (Figure S5). At subsolubilizing concentrations, we expect TX-100 to insert into the membrane bilayer, disturbing lipid packing and increasing fluidity without fully disrupting the intact vesicle. This partial solubilization then likely leads to the formation of intact donut-like toroidal structures as the membrane reorganizes to minimize edge energy while accommodating detergent-lipid micellar phases. In short, we hypothesize that this transformation reflects a transition between bilayer and mixed-micelle structures, driven by TX-100s ability to destabilize the bilayer architecture. We note that the SEM sample preparation involved using a thin (8 nm) conductive layer, but as previous studies indicate, this minimally alters the particle morphology.[35] Taken in conjunction with our single-particle FLIM data, the presented work is broadly supportive of a solubilization model that encompasses TX-100 induced vesicle swelling and morphological transitions, prior to complete micellization.

A remarkable outcome of this study is the demonstration that fluorescence dequenching can sensitively report on detergent-induced conformational expansion and morphological restructuring of individual intact vesicles in solution. Furthermore, these effects were observed at concentrations approaching the CMC, highlighting the capacity of nonionic detergents to induce significant structural rearrangements in highly curved vesicles. While the current data does not report on the initial dynamics of single TX-100 molecules directly interacting with the membrane, and further work in this area is highly desirable to quantify the precise mechanistic details of the initial interaction, our findings broadly support a model of TX-100 induced solubilization that involves structural remodelling of the intact vesicle prior to lysis. In this context, fluorescence dequenching is a powerful single-color alternative to dual-color FRET-based approaches, and opens a platform for enabling dynamic, nm-scale insights into membrane behavior without requirements for complex fluorophore pairing. Further advantages of the technique include its ability to operate across a range of fluorophores and surfactant conditions, and to enable interrogation of vesicle structure on a vesicle-by-vesicle basis, bypassing ensemble averaging which often obscures heterogeneous or transient events within vesicle populations.

Our data reveals that TX-100 induces vesicle swelling and the formation of nonspherical, toroidal-like structures prior to membrane rupture and the formation of mixed detergent-micelles. This multistep solubilization mechanism is consistent with previous observations in giant unilamellar vesicles (GUVs), where TX-100 was shown to induce long-lived pores and substantial vesicle shape changes.[36−39] Indeed, a direct comparison between the data obtained from large unilamellar vesicles and giant vesicles composed of POPC revealed common features after incubation with TX-100, including similar concentration requirements to achieve solubilization, morphological changes below the detergent's CMC, and evidence of the formation of toroidal-like structures (Figure S6). Both systems also displayed quenched initial lifetimes, biexponential decay behavior and an increase in average lifetime under matched detergent conditions. Interestingly, we identified that the half-maximal concentration for solubilization in the case of the giant vesicles was 0.18 ± 0.01 mM, which we note is in line with the value obtained from the vesicles of 30−1000 nm diameter. In both scenarios, the high curvature of the vesicles likely destabilizes upon detergent intercalation, leading to a reduction in membrane tension that facilitates global deformability and morphological transitions. This scenario aligns with theoretical models in which TX-100 - due to its amphipathic, flat wedge-like geometry and near-zero spontaneous curvature - intercalates symmetrically into the bilayer. Through flip-flop, lipid packing may then be compromised, membrane asymmetry disrupted and conditions become favorable for non spherical morphologies and, subsequently, mixed micelle formation. Irrespective, the fluorescence dequenching approach on highly curved, sub micron sized vesicles, is complementary to previous optical microscopy experiments involving giant unilamellar vesicles, and the combined data suggests a common general mechanism of solubilization.

Our findings also corroborate previous work that demonstrates that TX-100 perturbs local curvature and induces the

https://doi.org/10.1021/acsomega.5c10435
ACS Omega XXXX, XXX, XXX−XXX

formation of worm-like or tubular vesicles, invaginated forms, and other nonspherical intermediates.[37,38,40,41] Similarly, the observed structural transformations also echo earlier reports of TX-100—induced swelling and shape changes in chloroplast membranes and human red blood cells,[42,43] reinforcing the broader relevance of our observations. An important mechanistic implication of our study, however, is the observation that significant membrane deformations occur at lipid-to-detergent ratios of ∼2000:1—equivalent to <100 detergent monomers per vesicle. This supports the hypothesis that insertion and accumulation of individual TX-100 molecules, even at low concentrations below the CMC, can initiate conformational transitions.

It is also worth re-emphasizing the key advantages of the fluorescence dequenching approach. First, individual fluorescently tagged vesicles can be interrogated on a vesicle-by-vesicle basis thereby bypassing major limitations associated with ensemble averaging tools. Second, the assay operates well on the nanoscale, providing sensitivity comparable to FRET based measurements, but without the complexities associated with spectral overlap and bleed-through. Indeed, we have established that the combination of ensemble and single-vesicle spectroscopy approaches based on fluorescence dequenching can be used to reveal and monitor precise molecular level events that underpin detergent-induced vesicle solubilization in vitro, and we identify that TX-100 alters the structure of both freely diffusing and surface-immobilized vesicles via a mechanism comprising swelling and the formation of toroidal-like structures prior to complete solubilization. Our observations provide new mechanistic insight for how solubilizing detergents perturb and damage highly curved vesicles and may be directly relevant to biotechnological applications where conformational control and manipulation of the membrane is vital. We also expect the presented approach to find general utility for unveiling vesicle structural changes in response to perturbative agents, including additional surfactants, disruptive proteins and antiviral agents beyond the test cases highlighted here.

CONCLUSIONS

The combination of ensemble and single-vesicle fluorescence dequenching approaches provides a powerful platform to study detergent-induced membrane remodelling. By correlating population-averaged and single-vesicle responses, this framework enables quantitative evaluation of nanoscale structural transitions with molecular-level precision. The ability to quantify structural changes in vesicles in response to detergents at both the population and individual levels offers utility for studying the role of perturbative agents more broadly. Mechanistically, our results reveal that TX-100 induces substantial vesicle structural disruption at sub-CMC concentrations, where insertion of <100 molecules per vesicle is sufficient to trigger membrane swelling. We also found that vesicle size across a broad curvature range (30 nm to >1 μm) exerted minimal influence on the detergent−membrane interaction, with comparable half-maximal concentration constants observed for all diameters tested. Our single-vesicle imaging approaches further highlight a pronounced detergent-induced transition in which spherical vesicles morphologically alter into toroidal structures before complete solubilization. These observations refine the three-step solubilization model by linking early detergent−vesicle interactions to large-scale morphological transitions. This now opens potential implications for biotechnological applications where controlled membrane remodelling is desirable. We anticipate the toolbox presented here will also be valuable in assessing vesicle responses to other classes of molecular disruptors, including membrane-active peptides, surfactants, pharmacological agents and proteins with important biomedical significance.

ASSOCIATED CONTENT

Supporting Information

The Supporting Information is available free of charge at https://pubs.acs.org/doi/10.1021/acsomega.5c10435.

Time-resolved fluorescence data, representative FLIM and SEM images (PDF)

AUTHOR INFORMATION

Corresponding Author

Steven D. Quinn − *School of Physics, Engineering and Technology, University of York, York YO10 5DD, U.K.; York Biomedical Research Institute, University of York, York YO10 5DD, U.K.;* orcid.org/0000-0003-3442-4103; Email: steven.quinn@york.ac.uk

Authors

Claudia M. F. Andrews − *School of Physics, Engineering and Technology, University of York, York YO10 5DD, U.K.*

Christopher M. Hofmair − *School of Physics, Engineering and Technology, University of York, York YO10 5DD, U.K.*

Lauryn Roberts − *School of Physics, Engineering and Technology, University of York, York YO10 5DD, U.K.*

Emily James − *School of Physics, Engineering and Technology, University of York, York YO10 5DD, U.K.*

Katie Morris − *School of Physics, Engineering and Technology, University of York, York YO10 5DD, U.K.;* orcid.org/0000-0002-8944-2264

Kevin Kramm − *PicoQuant, Rudower, 12489 Berlin, Germany*

Mark C. Leake − *School of Physics, Engineering and Technology, University of York, York YO10 5DD, U.K.; Department of Biology and York Biomedical Research Institute, University of York, York YO10 5DD, U.K.;* orcid.org/0000-0002-1715-1249

Yue Wang − *School of Physics, Engineering and Technology, University of York, York YO10 5DD, U.K.;* orcid.org/0000-0002-2482-005X

Complete contact information is available at: https://pubs.acs.org/10.1021/acsomega.5c10435

Notes

The authors declare the following competing financial interest(s): Co-author K. K. is an employee of PicoQuant.

ACKNOWLEDGMENTS

The authors acknowledge the Engineering and Physical Sciences Research Council (EP/V034030/1 and EP/V047663/1) and Alzheimer's Research UK (RF2019-A-001) for support. We also thank Dr. Lara Dresser (University of York, UK) for help with initial exploratory work, Laser 2000 (Joshua Seagrave) and Picoquant GmbH for use of the Luminosa equipment, Prof. Daniella Barillá (University of York, UK) for use of DLS instrumentation, and the Bioscience Technology Facility at the University of York.

REFERENCES

(1) Garavito, R. M.; Ferguson-Miller, S. Detergents as tools in membrane biochemistry. *J. Biol. Chem.* **2001**, *276* (35), 32403−32406.
(2) Farcet, J. B.; Karbiener, M.; Zelger, L.; Kindermann, J.; Kreil, T. R. Detergent-Mediated Virus Inactivation in Biotechnological Matrices: More than Just CMC. *Int. J. Mol. Sci.* **2023**, *24* (9), 7920.
(3) Conley, L.; Tao, Y.; Henry, A.; Koepf, E.; Cecchini, D.; Pieracci, J.; et al. Evaluation of eco-friendly zwitterionic detergents for enveloped virus inactivation. *Biotechnol. Bioeng.* **2017**, *114* (4), 813−820.
(4) Stewart, M. P.; Langer, R.; Jensen, K. F. Intracellular Delivery by Membrane Disruption: Mechanisms, Strategies, and Concepts. *Chem. Rev.* **2018**, *118* (16), 7409−7531.
(5) Raoufi, E.; Bahramimeimandi, B.; Salehi-Shadkami, M.; Chaosri, P.; Mozafari, M. R. Methodical Design of Viral Vaccines Based on Avant-Garde Nanocarriers: A Multi-Domain Narrative Review. *Biomedicines* **2021**, *9* (5), 520.
(6) Chan, Y. H. M.; Boxer, S. G. Model membrane systems and their applications. *Curr. Opin. Chem. Biol.* **2007**, *11* (6), 581−587.
(7) Yadav, V.; Lunson, M.; Shore, H.; Aucamp, J. Systematic Development of a Detergent Toolbox as an Alternative to Triton X-100. *Biotechnol. Bioeng.* **2025**, *122* (5), 1096−1104.
(8) Koley, D.; Bard, A. J. Triton X-100 concentration effects on membrane permeability of a single HeLa cell by scanning electrochemical microscopy (SECM). *Proc. Natl. Acad. Sci. U.S.A.* **2010**, *107* (39), 16783−16787.
(9) Klammt, C.; Schwarz, D.; Fendler, K.; Haase, W.; Dotsch, V.; Bernhard, F. Evaluation of detergents for the soluble expression of alpha-helical and beta-barrel-type integral membrane proteins by a preparative scale individual cell-free expression system. *FEBS J.* **2005**, *272* (23), 6024−6038.
(10) Zhang, L.; Chai, X.; Sun, P.; Yuan, B.; Jiang, B.; Zhang, X.; Liu, M. The Study of the Aggregated Pattern of TX100 Micelle by Using Solvent Paramagnetic Relaxation Enhancements. *Molecules* **2019**, *24* (9), 1649.
(11) Singh, S. K.; Kishore, N. Thermodynamic insights into the binding of triton X-100 to globular proteins: A calorimetric and spectroscopic investigation. *J. Phys. Chem. B* **2006**, *110* (19), 9728−9737.
(12) Lichtenberg, D.; Ahyayauch, H.; Goni, F. M. The mechanism of detergent solubilization of lipid bilayers. *Biophys. J.* **2013**, *105* (2), 289−299.
(13) De la Maza, A.; Parra, J. L. Vesicle-micelle structural transition of phosphatidylcholine bilayers and Triton X-100. *Biochem. J.* **1994**, *303* (3), 907−914.
(14) Schnitzer, E.; Lichtenberg, D.; Kozlov, M. M. Temperature-dependence of the solubilization of dipalmitoylphosphatidylcholine (DPPC) by the non-ionic surfactant Triton X-100, kinetic and structural aspects. *Chem. Phys. Lipids* **2003**, *126* (1), 55−76.
(15) Patra, S. K.; Alonso, A.; Goni, F. M. Detergent solubilisation of phospholipid bilayers in the gel state: the role of polar and hydrophobic forces. *Biochim. Biophys. Acta* **1998**, *1373* (1), 112−118.
(16) Mattei, B.; Franca, A. D.; Riske, K. A. Solubilization of binary lipid mixtures by the detergent Triton X-100: the role of cholesterol. *Langmuir* **2015**, *31* (1), 378−386.
(17) Sudbrack, T. P.; Archilha, N. L.; Itri, R.; Riske, K. A. Observing the solubilization of lipid bilayers by detergents with optical microscopy of GUVs. *J. Phys. Chem. B* **2011**, *115* (2), 269−277.
(18) Muddana, H. S.; Chiang, H. H.; Butler, P. J. Tuning membrane phase separation using nonlipid amphiphiles. *Biophys. J.* **2012**, *102* (3), 489−497.
(19) Pizzirusso, A.; De Nicola, A.; Milano, G. MARTINI Coarse-Grained Model of Triton TX-100 in Pure DPPC Monolayer and Bilayer Interfaces. *J. Phys. Chem. B* **2016**, *120* (16), 3821−3832.
(20) Bandyopadhyay, S.; Shelley, J. C.; Klein, M. L. Molecular dynamics study of the effect of surfactant on a biomembrane. *J. Phys. Chem. B* **2001**, *105* (25), 5979−5986.
(21) Helenius, A.; Simons, K. Solubilization of membranes by detergents. *Biochim. Biophys. Acta* **1975**, *415* (1), 29−79.
(22) Dresser, L.; Graham, S. P.; Miller, L. M.; Schaefer, C.; Conteduca, D.; Johnson, S.; et al. Tween-20 Induces the Structural Remodeling of Single Lipid Vesicles. *J. Phys. Chem. Lett.* **2022**, *13* (23), 5341−5350.
(23) Dalgarno, P. A.; Juan-Colas, J.; Hedley, G. J.; Pineiro, L.; Novo, M.; Perez-Gonzalez, C.; Samuel, I. D. W.; Leake, M. C.; Johnson, S.; Al-Soufi, W.; et al. Unveiling the multi-step solubilization mechanism of sub-micron size vesicles by detergents. *Sci. Rep.* **2019**, *9* (1), 12897.
(24) Juan-Colas, J.; Dresser, L.; Morris, K.; Lagadou, H.; Ward, R. H.; Burns, A.; et al. The Mechanism of Vesicle Solubilization by the Detergent Sodium Dodecyl Sulfate. *Langmuir* **2020**, *36* (39), 11499−11507.
(25) Dresser, L. G.; Kunstmann-Olsen, C.; Conteduca, D.; Hofmair, C. M.; Smith, N.; Clark, L.; Johnson, S.; Penedo, J. C.; Leake, M. C.; Quinn, S. D. Multiple intermediates in the detergent-induced fusion of lipid vesicles. *Commun. Mater.* **2024**, *5* (1), 195.
(26) Leavesley, S. J.; Rich, T. C. Overcoming Limitations of FRET Measurements. *Cytometry, Part A* **2016**, *89a* (4), 325−327.
(27) Stetefeld, J.; McKenna, S. A.; Patel, T. R. Dynamic light scattering: a practical guide and applications in biomedical sciences. *Biophys. Rev.* **2016**, *8* (4), 409−427.
(28) Schrimpf, W.; Barth, A.; Hendrix, J.; Lamb, D. C. PAM: A Framework for Integrated Analysis of Imaging, Single-Molecule, and Ensemble Fluorescence Data. *Biophys. J.* **2018**, *114* (7), 1518−1528.
(29) Luchini, A.; Vitiello, G. Mimicking the Mammalian Plasma Membrane: An Overview of Lipid Membrane Models for Biophysical Studies. *Biomimetics* **2020**, *6* (1), 3.
(30) Leake, M. C.; Quinn, S. D. A guide to small fluorescent probes for single-molecule biophysics. *Chem. Phys. Rev.* **2023**, *4* (1), 011302.
(31) Gullapalli, R. R.; Demirel, M. C.; Butler, P. J. Molecular dynamics simulations of DiI-C18(3) in a DPPC lipid bilayer. *Phys. Chem. Chem. Phys.* **2008**, *10* (24), 3548−3560.
(32) Lubart, Q.; Hannestad, J. K.; Pace, H.; Fjallborg, D.; Westerlund, F.; Esbjorner, E. K.; et al. Lipid vesicle composition influences the incorporation and fluorescence properties of the lipophilic sulphonated carbocyanine dye SP-DiO. *Phys. Chem. Chem. Phys.* **2020**, *22* (16), 8781−8790.
(33) Knoch, H.; Ulbrich, M. H.; Mittag, J. J.; Buske, J.; Garidel, P.; Heerklotz, H. Complex Micellization Behavior of the Polysorbates Tween 20 and Tween 80. *Mol. Pharmaceutics* **2021**, *18* (8), 3147−3157.
(34) Schäfer, K.; Kolli, H. B.; Killingmoe Christensen, M.; Bore, S. L.; Diezemann, G.; Gauss, J.; Milano, G.; Lund, R.; Cascella, M. Supramolecular Packing Drives Morphological Transitions of Charged Surfactant Micelles. *Angew. Chem., Int. Ed.* **2020**, *59* (42), 18591−18598.
(35) Chuo, S. T.; Chien, J. C.; Lai, C. P. Imaging extracellular vesicles: current and emerging methods. *J. Biomed. Sci.* **2018**, *25* (1), 91.
(36) Yandrapalli, N.; Seemann, T.; Robinson, T. On-Chip Inverted Emulsion Method for Fast Giant Vesicle Production, Handling, and Analysis. *Micromachines* **2020**, *11* (3), 285.
(37) Casadei, B. R.; Domingues, C. C.; de Paula, E.; Riske, K. A. Direct visualization of the action of Triton X-100 on giant vesicles of erythrocyte membrane lipids. *Biophys. J.* **2014**, *106* (11), 2417−2425.
(38) Mattei, B.; Lira, R. B.; Perez, K. R.; Riske, K. A. Membrane permeabilization induced by Triton X-100: The role of membrane phase state and edge tension. *Chem. Phys. Lipids* **2017**, *202*, 28−37.
(39) Drab, M.; Pandur, Z.; Penic, S.; Iglic, A.; Kralj-Iglic, V.; Stopar, D. A Monte Carlo study of giant vesicle morphologies in non-equilibrium environments. *Biophys. J.* **2021**, *120* (20), 4418−4428.
(40) Bjornestad, V. A.; Lund, R. Pathways of Membrane Solubilization: A Structural Study of Model Lipid Vesicles Exposed to Classical Detergents. *Langmuir* **2023**, *39* (11), 3914−3933.
(41) Pizzirusso, A.; De Nicola, A.; Sevink, G. J. A.; Correa, A.; Cascella, M.; Kawakatsu, T.; et al. Biomembrane solubilization mechanism by Triton X-100: a computational study of the three stage model. *Phys. Chem. Chem. Phys.* **2017**, *19* (44), 29780−29794.

https://doi.org/10.1021/acsomega.5c10435
ACS Omega XXXX, XXX, XXX−XXX

(42) Karabaliev, M.; Paarvanova, B.; Savova, G.; Tacheva, B.; Georgieva, R. In Situ Monitoring of Morphology Changes and Oxygenation State of Human Erythrocytes During Surfactant-Induced Hemolysis. *Cells* **2025**, *14* (7), 469.
(43) Habibi, S.; Lee, H. Y.; Moncada-Hernandez, H.; Gooding, J.; Minerick, A. R. Impacts of low concentration surfactant on red blood cell dielectrophoretic responses. *Biomicrofluidics* **2019**, *13* (5), 054101.

https://doi.org/10.1021/acsomega.5c10435
ACS Omega XXXX, XXX, XXX−XXX